ELSEVIER

International Journal of Mass Spectrometry 213 (2002) 25–44

www.elsevier.com/locate/ijms

Surface induced dissociation of chromium hexacarbonyl on fluorinated alkanethiolate surface in ion cyclotron resonance mass spectrometer: studies of energetics of the process using recursive internal energy distribution search method

V.S. Rakov[a], E.V. Denisov[a], J.H. Futrell[a,*], D.P. Ridge[b]

[a]*Pacific Northwest National Laboratory, William R. Wiley, Environmental Molecular Science Laboratory, Richland, WA*
[b]*University of Delaware, Newark, DE*

Received 6 December 2000; accepted 27 July 2001

Abstract

Energy transfer in ion-surface collisional activation is characterized for 0–30 eV collisions of chromium hexacarbonyl molecular cations with a monolayer of fluorinated alkanethiolate self-assembled onto a solid gold surface. This surface was mounted on the back trapping plate of the Infinity® cell of a Bruker BioApex 7T ion cyclotron resonance mass spectrometer on the B-field axis orthogonal to the ion beam direction. Internal energy deposition was deduced from fragmentation spectra using a recursive internal energy distribution search method. The efficiency of energy transfer into the ion slowly increases with incident ion energy to a maximum value of 20% at about 23 eV collision energy. Approximate kinetic energy distributions of the fragments were measured by deducing the dependence of ion abundance on trapping potential. From the kinetic energy dependence on mass we infer that rapid decomposition of the molecular cation occurs after it recoils from the surface. Knowledge of both internal and kinetic energy distributions of collisionally activated ions enabled us to deduce the energy deposited into the self-assembled monolayer as a function of collision energy. (Int J Mass Spectrom 213 (2002) 25–44) © 2002 Elsevier Science B.V.

Keywords: Surface induced dissociation; Ion cyclotron resonance; Self-assembled monolayers; Internal energy deposition; Fragment kinetic energy

1. Introduction

The most important parameter for characterizing collisional activation in tandem mass spectrometry is the energy transfer function. The objective of the present research is to deduce the energy transfer function for surface induced dissociation (SID) [1]. SID is rapidly emerging as a viable alternative to multiple collision activation of complex molecules but very little quantitative information on the dependence of the energy transfer function on collision energy is available. In the present research we describe a new Fourier transform mass spectrometry (FTMS)/SID apparatus for which we have utilized a recursive internal energy distribution search (RIEDS) method [2] to establish the internal energy of activated ions from their fragment ion spectrum. The

* Corresponding author. E-mail: jean.futrell@pnl.gov

PII S1387-3806(01)00505-X

thermometer molecule chromium hexacarbonyl was used to evaluate both instrument performance and our data analysis methods. The axial kinetic energies of both the parent and all fragment ions were measured in these experiments. Combining this information enables us to draw conclusions about energy transfer in the excitation step and energy disposal into the surface. These experiments provide the basis for further work on SID activation of complex molecular ions.

A few studies of SID using modified crossed-beams instruments and varied-collision/detection-angle multipole MS and time-of-flight (TOF) MS setups have provided information on the dependence of fragmentation mechanisms, patterns, and fragment translational energy on scattering angle, collision energy, nature of projectile, and structure of the surface [3–8]. Theoretical modeling of these phenomena [9,10] has provided additional insights into SID dynamics. Nevertheless the variation of ionization conditions, angle of incidence, time scale, and product ion collection efficiency in various experimental studies of SID make results strongly instrument/method dependent.

Early FT ion cyclotron resonance (ICR) SID experiments have reported the fragmentation patterns of small to medium size molecular ions. Ijames and coworkers [11–13] used a double-cell FT ICR instrument to examine SID resulting from glancing collision on stainless steel trapping electrodes. In these experiments isolated parent ions were excited by cyclotron resonance and then allowed to collide with a trapping plate by briefly reducing the trapping voltage. Later Chorush and coworkers [14] performed similar SID experiments with a copper surface in an open-cell FT ICR configuration. Kinetic energy and impact angle of the ions were poorly defined in these experiments. Both experimental approaches suffered from significant ion losses, resulting from both ion neutralization and magnetron diffusion. The present experiments provide better control of activation parameters and justify a more detailed analysis of energy transfer.

Recent SID experiments have utilized monolayers of alkanethiolate molecular chains self-deposited onto a vapor-deposited polycrystalline gold substrate [15–19]. These self-assembled monolayers (SAMs) form trans-zig-zag domain structures tilted at 30 ± 0.5 degrees with respect to the surface normal [20–22]. When used as targets in SID, they significantly outperform conductive solid surfaces [15,17,18]. Projectile ion neutralization is suppressed by the uniform coating of the conductor by insulating SAMs, while surface reactivity is suppressed by using fluorinated alkanethiolates. The chain length is chosen sufficiently short to minimize surface charging but long enough to suppress neutralization. Preliminary experiments carried out in our laboratory investigated normal incidence SID of benzene on fluorinated alkanethiolate (FC_{12}) surfaces deposited on gold. This was done using a 3T Finnigan FTMS-2000 instrument with a continuous external ion source [23]. That experimental setup served as the prototype for designing the present experimental configuration [24], which has a Bruker BioApex 7T FT ICR as the instrumental platform.

The combination of normal incidence ion impact in a higher magnetic field than in previous work both minimizes radial defocusing and enables higher collection efficiency. Utilizing fluorinated SAM targets significantly reduces both surface neutralization and reactions and enhances energy transfer into the parent ion [18]. The most reliable measure of SAM quality is the parent-to-fragments conversion ratio defined as $\Sigma I_{SID}/\Sigma I_{parent}$, [where I_{SID} was the sum of all the ions detected after the SID took place, and I_{parent} represented total ion abundance observed with 0 V source offset, (the “no SID” case)]. For 30 eV SID the parent-to-fragment conversion ratio was of the order of 30% on fresh SAMs and slowly declined with use. Routine bakeouts for 20 h at 80–90 °C typically destroyed the SAM structure, reducing the ratio below 0.1%; this ratio is comparable to that obtained on uncoated gold surfaces (which are actually covered with a thin film of organic oil in MS systems fitted with oil diffusion pumps).

In SID internal energy of the precursor is increased by collision with a stationary solid surface at a moderate and well-controlled kinetic energy. If excitation and statistical redistribution of energy within

the activated precursor ion is fast relative to decomposition the unimolecular dissociation of the excited ion is rate-limiting and the observed mass spectrum of fragment ions depends only on energy deposited into the precursor ion and the time between excitation and detection of fragments. The connection between the observed fragment ion spectrum and internal energy of the parent ion is provided by its breakdown graph—the fragment ion abundance at a specific postexcitation time as a function of internal energy. Breakdown graphs can be determined experimentally using methods such as photoelectron photoion coincidence (PEPICO) spectrometry or can be calculated theoretically. PEPICO breakdown graphs necessarily refer to the characteristic sampling time of the order of several microseconds between ion excitation and fragment detection.

For most small molecules and explicitly for the thermometer molecule chromium hexacarbonyl used as our test molecule all dissociations are so rapid for any internal energy above threshold that breakdown curves are quasitime-independent. Since fragmentation of $Cr(CO)_6^+$ into $Cr(CO)_n^+$ ions in sequential reactions eliminating CO involves very little entropy of activation all the reactions in the reaction sequence proceed rapidly. Consequently, breakdown graphs measured on a microsecond time scale in PEPICO experiments [25] can be directly used to interpret results obtained on the millisecond time scale of our FTMS experiments. It therefore follows that the observed mass spectrum can be used in combination with the parent ion's PEPICO breakdown graph to define the internal energy distribution of the activated precursor ion. Specifically, the breakdown graph and energy-dependent fragmentation patterns are the input data for the RIEDS method [2] used in this work. An internal energy distribution computed by RIEDS optimizes the agreement between predicted and observed mass spectra.

2. Instrumental methods

The University of Delaware Bruker BioApex 7T FT ICR instrument used in these studies is shown schematically in Fig. 1 along with a timing diagram for a typical ICR-SID experiment utilizing dynamic voltage trapping (DVT) [26]. The modular components are the source block, the ion transfer optics and the ICR cell detector, and the SID surface target. The ICR experiment was controlled by an SGI data station using the XSPEC software package and Bruker's XMASS user interface.

The electron impact (EI) source assembly consists of the source block, the repeller electrode, the filament, and the extraction lens pair. Typical values for the lens potentials used in EI experiments are listed in Table 1, along with controls for each of these parameters. Chromium hexacarbonyl was evaporated from an electrically isolated heated solid probe inserted into the source block assembly and ionized by 18 eV electron impact. This ionization energy is a compromise dictated by rapidly decreasing signal at lower electron energies and extensive fragmentation that occurred prior to SID at higher energies. The ions were constantly extracted by the potential applied to a pair of extraction lenses into the ion optics guide. Modulation of the ion beam produced in the EI source was accomplished using the ion deflector lens pairs of the ion transfer optics to gate the ion beam. The electrostatic ion guide was functionally described previously [24].

The SID target was positioned just inside the ICR cell in electrical contact with the back trapping plate. A copper holder with 1 cm diameter base and 0.5 cm diameter pin had a solid gold disk, also 0.5 cm in diameter, soldered onto the pin. This assembly extended about 1.5 mm into the ICR cell volume through the rear trapping aperture. Thus no copper surface was "exposed" to the ions. The preparation procedure for bounding and annealing FC_{12} alkanethiolate $[CF_3(CF_2)_9C_2H_4SH]$ SAM on the target was previously reported [24].

Neither collisional cooling nor Side-Kick™ trapping of ions as they enter the ICR cell are entirely satisfactory for SID experiments. Enhancement of magnetron motion by Side-Kick trapping introduces uncertainty in the radial coordinate of surface collision and the SID angle of incidence. Collisional trapping increases the dispersion in ion-surface colli-

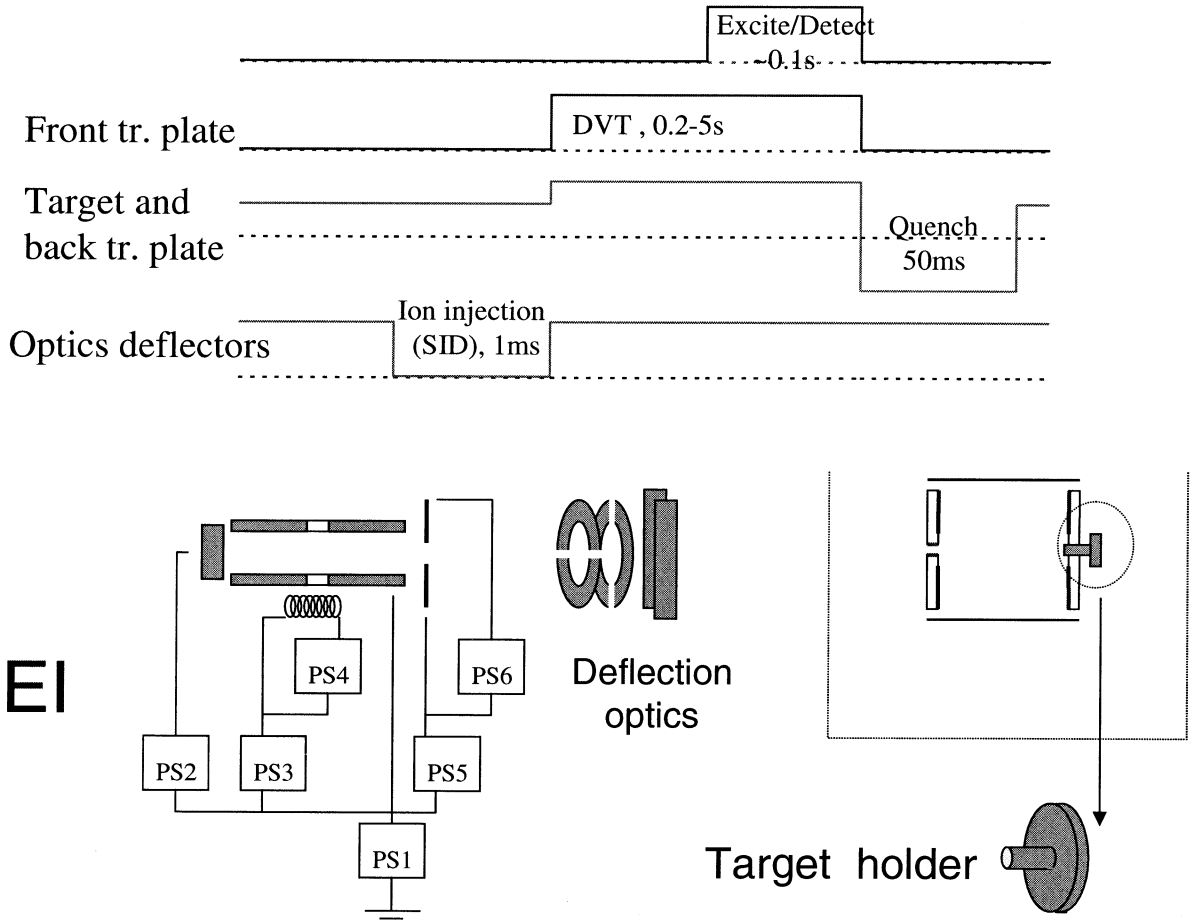

Fig. 1. Schematic view of the University of Delaware ICR SID instrument and a typical experimental event sequence. Key functional units of the instrument are the voltage-isolated external ion source, electrostatic ion guide, infinity ICR cell capable of DVT, and the SAM target assembly.

sion energy, introduces additional axial-mode collision-induced dissociation (CID) fragmentation and requires time-consuming pumpdown of collision gas prior to ICR excitation and detection. For these reasons we chose DVT to capture ions in the cell in the present research. In this procedure the trapping plate of the ICR cell closest to the source (front plate) is initially at ground potential and the back plate is held at 3 volts above the ion source potential. Thus low energy parent ions enter the cell, stop a short distance from the back plate and reverse their trajectory inside the cell. Lifting the potential on the front trapping plate at an appropriate time traps all (or most) of the ions inside the cell. Excitation and detection follow. For SID experiments the potential of the entire ion source is lifted above ground to impact ions on the surface with a chosen kinetic energy. Fragment ions recoil from the surface and are captured

Table 1
Electron impact ionization source elements: settings and controls

Element	Control	Value
Ion repeller	PS2	5 V
Source block	PS1	3 V
Extraction pair centerline	PS5	0 V
Extraction pair difference	PS6	0 V
Electron energy	PS3	18 V
Filament current	PS4	3 A

by a chosen trapping potential after a steady state population of ions is established in the cell. It should be noted, however, that our experiment cannot be "tuned" to maximize intensities of parent ions and fragments simultaneously. In experiments reported here we established a compromise which efficiently captures those two different populations simultaneously. These conditions do not maximize intensities for either the parent or fragment ions [24].

The kinetic energy distribution of the parent ions was measured by a variation of the retarding potential method. Prior to the trapping step the potential of the front trapping plate was systematically varied while the source block and extraction pair were held at 3 volts (for parent ion injection). Ions were pushed out of the source by holding the repeller plate at 5 volts. The back trapping plate was held at 10 volts with respect to the grounded ICR cell, retarding all the parent ions and reversing their trajectories. After an equilibrium distribution of ions was established inside the cell (less than 1 ms), both the front and back trapping plate potentials were switched to 10 volts. This was followed by excitation and detection of parent ions and by cell quench. When plotted as a function of the front trapping plate potential prior to DVT the parent ion abundance curve had a characteristic S-shape, whose inflection point approximately equals the parent ion most probable kinetic energy.

SID fragment ions were found to have relatively low kinetic energy at all collision energies. A slight variation of the retarding potential technique was used in combination with additional mathematical modeling to deduce their kinetic energies. Prior to ICR excitation and detection of the fragment ions the front and the back trapping plates of ICR cell were kept at 0 and 3 volts, respectively, while the projectile ion beam impacts the SAM. Parent ion beam pulses of the order of 1 ms were used which can be considered long compared to parent ion TOF and the travel time of the fragment ions away from the SAM through the ICR cell. Thus a steady-state distribution of the fragment ions inside the cell is assumed prior to ICR excitation and detection. After the steady-state axial distribution of undissociated parent and fragment ions was established DVT was activated by switching both trapping plates to the same potential above 3 volts. Experimental spectra were obtained for a range of trapping voltages. Relative ion abundance at various trapping conditions was used to deduce kinetic energy of the fragment ions using formalism outlined in Sec. 3B and described in detail in Appendix.

3. Results and discussion

3.1. Deducing the internal energy distribution of parent ions from the fragmentation spectrum; the recursive internal energy distribution search (RIEDS) algorithm

Several methods have been proposed for estimating the internal energy of the predissociating parent ion based on its subsequent fragmentation. The simplest method, introduced by Wysocki and coworkers [27] is based on the fact that for a reaction sequence $A_0 \rightarrow A_1 \rightarrow \ldots \rightarrow A_n \rightarrow \ldots \rightarrow A_N$, no A_n fragment can be formed from A_0 parent unless its internal energy exceeds its threshold energy E_n. Additionally, all A_0 parents with internal energies in the range of $[E_n, E_{n+1}]$ will fragment into A_n. Based on this assumption, the intensity of the A_n fragment is taken to be proportional to the product of the energy band width, $(E_{n+1} - E_n)$ and the relative number of activated parent ions with internal energy in this range, P_n, given by $P_n = [A_n]/(E_{n+1} - E_n)$. This P_n value is taken as proportional to the probability that the activated parent ion has internal energy $E_n + 0.5[E_{n+1} - E_n]$. This "one energy - one fragment" method assumes that the breakdown curves are rectangular and only the A_n fragment is produced from parent ion in the internal energy range between the appearance of A_n, E_n, and the next higher A_{n+1} fragment appearance energy, E_{n+1}. A characteristic feature of this method is that the number of peaks in the spectrum limit the rank of the **P** vector. If the spectrum has m peaks, then $n \epsilon \{1,2, \ldots m\}$, and P_n value can be calculated at only m points. The predicted energy distribution has a rank of m, the number of fragments.

Vekey and coworkers [28,29] developed a "deconvolution" method which they tested on benzene,

pyridine, and acetone molecular ions. This method accounts for the fact that breakdown curves are not rectangular. The energy scale is divided into bins or energy regions. All ions formed with internal energy within a given bin are assumed to generate the same fragment spectrum. The spectrum predicted for each bin is determined by integrating the curves in the breakdown graph over that energy range (bin). A normalization procedure then derives from the observed spectrum the fraction of the activated precursor ions with internal energies within each energy bin. These fractions are taken as a measure of internal energy distribution function in the midpoint of the corresponding energy bins. Because it accounts for overlapping, nonrectangular curves the deconvolution method is an improvement over the "one energy - one fragment" method. However, since the number of bins cannot exceed the number of fragments the number of points in the energy distribution function is also limited by the number of peaks in the mass spectrum.

Beck et al. used an alternative method to recover the information on the internal energy of fullerenes in SID on highly oriented pyrolitic graphite surfaces [5]. In that work a Gaussian distribution of internal energy was assumed and optimized to predict the fragmentation spectrum which provided best correlation with experiment. A similar approach is realized by our recursive internal energy search method [2] which is discussed herein in detail. The RIEDS can be applied to any fragmentation $A_0 \rightarrow A_1, A_2, \ldots A_n, \ldots A_N$ for which the probability of formation of the A_n, ($n\epsilon\{1,2, \ldots N\}$) fragment is known as a function of internal energy of A_0. The method uses complete breakdown graphs (either estimated theoretically or obtained from PEPICO). A parametrized internal energy distribution function P(E) is estimated and combined with the breakdown curves to give a predicted spectrum of relative abundances of A_0 and $A_1, \ldots A_N$. The discrepancy between the predicted and observed spectrum is minimized by iterative adjustment of parameters defining the internal energy distribution function.

If the reference breakdowns curves are continuous, this procedure gives a continuous energy distribution function consistent with the observed spectrum rather than a function of rank N or N-1. Specifically, the energy distribution function of a parent ion is assumed to be of a known analytical form, *P(E)*, with the set of parameters, $\{c_m\}$, m = {1, M}, M < N. The probability of detecting A_n is proportional to the intensity of the n^{th} fragment in the spectrum, which is given by

$$I_n^{pr} \sim \int P(E) F_n(E) dE, \tag{1}$$

where $F_n(E)$ is the breakdown curve for the n^{th} fragment. Thus, for each trial *P(E)* internal energy distribution function, we create the $\{I_n^{pr}\}$ set of predicted spectral fragment intensities (predicted spectrum).

Minimizing the squared-residual sum,

$$Q = \sum_{r=0}^{lv} (I_n^{exp} - I_n^{pr})^2, \tag{2}$$

where $\{I_n^{exp}\}$ is the experimental spectrum set of intensities, against the $\{c_m\}$ parameters of the *P(E)* function, gives the energy distribution function, *P(E)* which minimizes the difference between $\{I_n^{exp}\}$ and $\{I_n^{pr}\}$. In this approach, *P(E)* is treated as a discrete functional, and the only limitations on the resulting *P(E)* are those fixed by choosing the defined analytical form for the internal energy distribution.

A broad variety of physically meaningful analytical forms can be used as the trial function for internal energy distribution. The only formal limitation is that the number of parameters, M is smaller then the overall number of fragments, N. In this study we used an "asymmetric Gaussian"

$$P(E) = \frac{1}{\sqrt{2\pi}\sigma} e^{\frac{(E^k - E_0)^2}{2\sigma^2}}, [\sigma, E_0, k] - \text{parameters}, \tag{3}$$

functional as a model for internal energy distributions. It is constructed by nonlinear scaling of the abscissa of a normal probability distribution, where the *k* parameter serves as a Gaussian asymmetry coefficient. When *k* is less than 1 in *P(E)*, the left shoulder

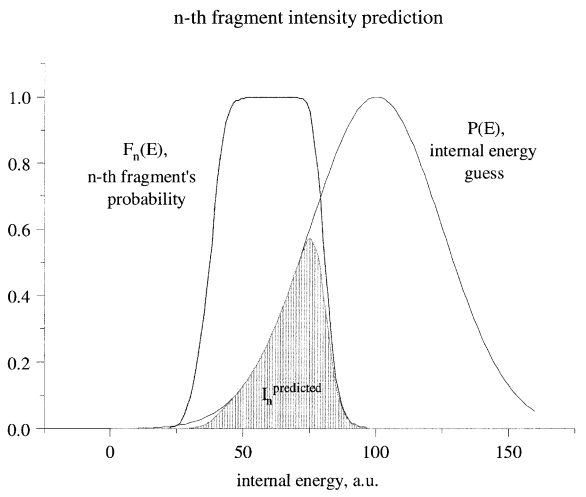

Fig. 2. Illustration of the RIEDS definition of prediction of intensity of a chosen fragment ion ($I_n^{predicted}$) from the parent ion with internal energy distribution *P(E)*. $F_n(E)$ is the curve for the nth fragment on a breakdown graph.

of the "bell" curve is steeper than the right one; when k is greater than one, the converse is true.

Application of the RIEDS algorithm is illustrated in Fig. 2. The function $F_n(E)$ represents the abundance of the n^{th} fragment in the spectrum as a function of internal energy (one-fragment curve from a breakdown graph). The internal energy distribution functional *P(E)* used in this illustration is Gaussian for simplicity. Since breakdown curves are scaled so that the cumulative probability of all fragments is unity for each energy, the $F_n(E)$ value can never exceed 1. The integral of the product $F_n(E)*P(E)$ is equal to the shaded area under the curve and is marked as $I_n^{predicted}$. This is the predicted spectral intensity of the A_n product. Similarly, for the next fragment, A_{n+1}, the predicted spectral intensity will be given by the $F_{n+1}(E)*P(E)$ product [with the same *P(E)*] integrated over energy. The spectrum predicted as a set of ion intensities for all the fragments using this particular trial function *P(E)* is constructed in this way. The difference between the predicted spectrum and the experimental one (the *Q* function defined above) is minimized against the set of parameters of the *P(E)* function using a SIMPLEX search minimization algorithm [30].

The RIEDS method is a completely general means for estimating the parent ion internal energy distribution responsible for the fragment spectrum generated in any particular experiment. It requires only that reaction-time-adjusted breakdown curves be available for the system of interest and takes full advantage of the information provided by the reference breakdown graphs. Although only N points (number of peaks in the spectrum) are available in each experiment (spectrum) fit the deduced internal energy distribution function is essentially continuous, having the same rank as the reference breakdown curves. The method also provides in Q a simple, objective measure of the success of a particular internal energy distribution in predicting the observed spectrum.

Nevertheless there is an effective upper limit which is realized mathematically in fitting the internal energy distribution. Namely, there is no sensitivity of the fit to experimental parameters when fragmentation is so nearly complete that it no longer changes with internal energy in numerical sense. This corresponds to the saturation of k(E) curves in the microcanonical ensemble (RRKM) treatment or to infinite temperature for thermal kinetics. It should also be noted that some knowledge about the form of the distribution is assumed in the choice of the *P(E)* function. For example, in Beck's work [5], the Gaussian distribution was assumed for internal energy of C_n^+ ($n \geq 60$) in SID on (HOPG) which provided good correlation between experimental and calculated spectra. Zhang used a linear combination of two Gaussians to interpret energy distributions in exothermic charge exchange reactions of $Fe(CO)_5^+$ with atomic and diatomic molecular ions [2]. This treatment correctly describes dissociation originating from two discrete electronic hypersurfaces. Since there is no a priori reason to anticipate that $Cr(CO)_6^+$ should be collisionally activated to excited electronic states the asymmetric Gaussian function is a reasonable choice for the present study. Alternative forms were investigated briefly and did not provide a better fit to experimental data.

The essence of the RIEDS algorithm and its application are illustrated by Fig. 3–5. Fig. 3(a) is a plot of normalized intensities of parent and fragment

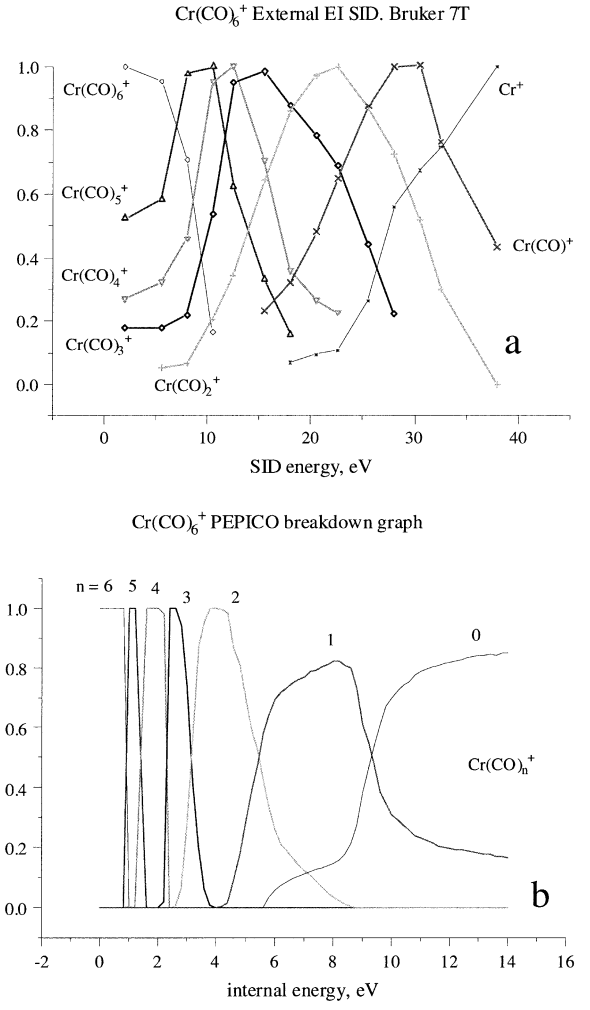

Fig. 3. Fragmentation of $Cr(CO)_6^+$. (a) SID fragmentogram; (b) PEPICO breakdown graph.

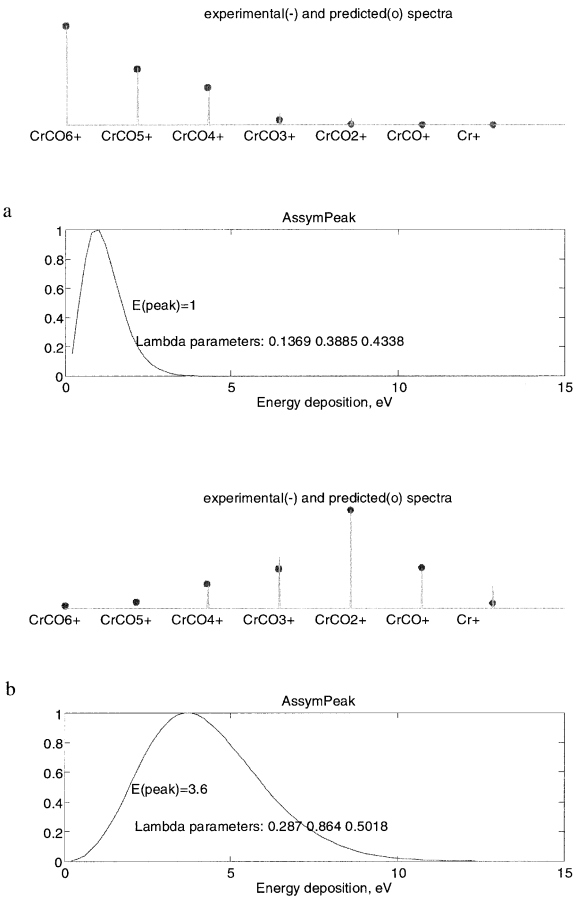

Fig. 4. Two screen-outputs of the RIEDS program: (a) 8 eV SID; (b) 20.5 eV SID. In both (a) and (b), the top plots show experimental (line) versus calculated (dot) spectra and the bottom graphs show the internal energy distributions which lead to the calculated spectra. Most probable values for the IE are shown as E(peak), lambda parameters are the current parameters of *P(E)* function.

ions from $Cr(CO)_6^+$ SID as a function of collision energy. It qualitatively resembles the PEPICO breakdown curve [25] for this compound shown in Fig. 3(b) which was used in RIEDS as a reference breakdown graph. Fig. 4 shows the individual fits of spectra at 8 (a) and 20.5 eV (b) SID collision energies. In both cases, the upper graph depicts both experimental (solid line) and predicted (hollow circles) spectra [note that the *m/z* "axis" is reversed (declining mass, increasing energy) in Fig. 4 to illustrate the "increase of fragmentation"]. The lower graphs in both (a) and (b) show the estimated internal energy distributions, which gave the calculated spectra (hollow circles in the upper plots). As shown in the two examples illustrated in Fig. 4 the experimental spectrum can be modeled accurately; the RIEDS-modeled spectra differed from the experimental ones (in terms of ratio of the residual-module sum over the sum of fragment intensities) by less then 4%.

Fig. 5 presents internal energy distributions for chromium hexacarbonyl at several SID collision energies deduced by RIEDS method. The maximum of the *P(E)* curve shifts towards higher energy and broadens as SID energy increases. The most probable

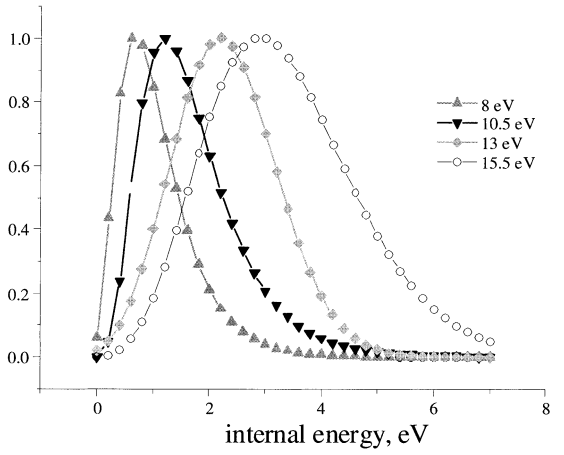

Fig. 5. Individual internal energy distributions obtained by RIEDS for $Cr(CO)_6^+$ SID at different collision energies normalized to unit peak intensity. Collision energy is specified in the legend.

values of the internal energy are plotted as a function of SID energy in Fig. 6 (a), where the broadening of the distributions is given by the width of the bars in the vertical axis. The x-axis "error bar" depicts the uncertainty [full width at half-maximum (FWHM)] of 2 eV in assignment of SID collision energy, deduced in the evaluation of primary ion kinetic energy discussed later.

Ignoring both the uncertainty in SID collision energy and the broadening of the internal energy distribution a respectable straight line could be drawn through the data points plotted in Fig. 6. Not shown in the figure, such a straight line infers that SID energy transfer efficiency is about 20%, in good agreement with the studies which postulated constant energy-transfer efficiency [27,31]. The negative intercept of such a linear plot is unacceptable in that it suggests negative internal energy in the ion or an error in kinetic energy deduced from retarding potential method. However, it must be noted that there is no physical reason to expect constant energy transfer efficiency for all projectile ions and SID targets. In fact, theoretical modeling suggests an increase in the energy transfer efficiency with increase in collision energy in the low energy range and its decline at higher energies [9,10]. In experimental studies for a variety of projectile ions and SID targets some of the

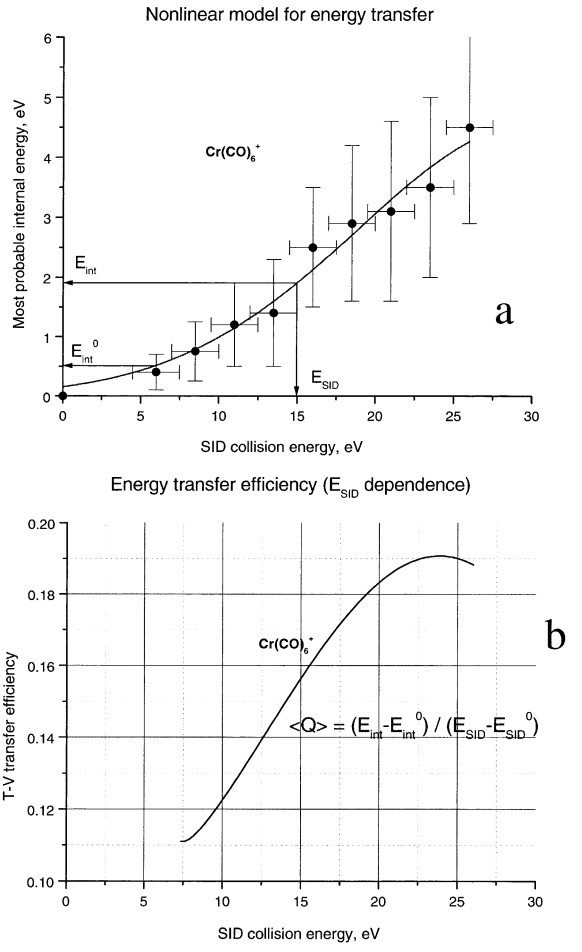

Fig. 6. T-V energy transfer in the SID of $Cr(CO)_6^+$; (a) the proposed nonlinear fit for the T-V transfer. Experimentally determined FWHM of 3 eV of parent ion SID collision energy is reflected as "error" bars on the x axis, while the widths of internal energy distributions calculated by RIEDS (see Fig. 5) are plotted as the y-axis "error" bars around the mode internal energy; (b) is the efficiency of the T-V transfer, with origin-of-coordinate correction (see the text).

observed $E_{int}(E_{coll})$ curves—even where explicitly reported as linear—show clear evidence for the predicted efficiency decrease at high SID energies [5,7,8,10,27]. For this reason we present as our preferred interpolation the nonlinear fit shown in Fig. 6(a). This figure suggests a slow to moderate increase in T-V conversion efficiency at low E_{SID} with gradual leveling at higher SID energy. We note that in this treatment of the data internal energy extrapolates to a

positive value (E_{SID}^0 = 0.1 eV) at zero SID energy; this implies that the parent ions formed by electron impact ionization have modest average internal excitation. This initial excitation value (E_{SID}^0) was subtracted from the internal energy in defining the SID T-V conversion efficiency. Thus, the first meaningful experimental point considered in our treatment is (E_{SID}^0, E_{int}^0) = (6 eV, 0.5 eV).

It is important to note that the bars in Fig. 6 (a) are not to be interpreted as error bars in any conventional sense. Rather they are the kinetic energy distribution widths (FWHM) of our reactant ion beam (abscissa) and the half-maximum widths of the internal energy distributions (ordinate). The nonlinear fit ε_{SID} (ε_{int}) of Fig. 6(a) is further analyzed in Fig. 6(b) by defining the T-V transfer efficiency as ($\varepsilon_{SID} - E_{SID}^0$)/($\varepsilon_{int} - E_{int}^0$) which corresponds geometrically to differentiation of Fig. 6(a) after a simple coordinate-origin adjustment. Fig. 6(b) presents the T-V transfer efficiency; it indicates that the maximum T-V transfer efficiency of about 19% is reached at about 23 eV collision energy. Obviously differentiation amplifies errors in the nonlinear curve and we cannot claim that the result is quantitatively accurate. Nevertheless the increase of collision efficiency just above threshold and its leveling at higher energy are probably reliable inferences from the data. We consider that they support theoretical modeling described previously [9,10] and agree with the expected behavior for energy transfer in SID.

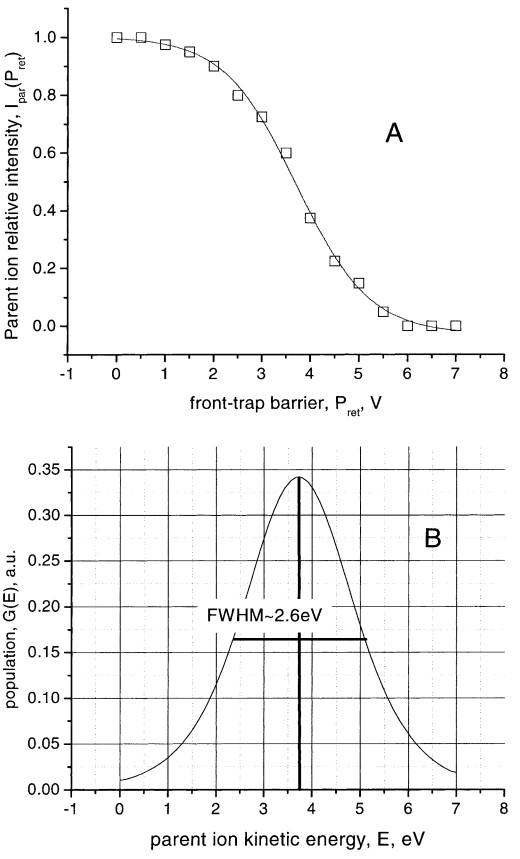

Fig. 7. Kinetic energy distributions (KEDs) of the parent ion. The source offset was 3 eV. The front trapping plate was kept at various potential levels and the DVT level was 10 volts: (a) shows ion abundance as a function of intermediate barrier height; (b) shows the KED deduced from (a). The FWHM of KED (unchanged with source offset) was used in plotting results in Fig. 6 (a).

3.2. Kinetic energy distributions (KEDs) of SID projectile and fragment ions; motion of ions in dynamic voltage trapping (DVT)

The kinetic energy distribution of parent ions was measured by the retarding potential (intermediate potential barrier) method as described in Section 2: Instrumental methods. Typical results are given by Fig. 7(a) which plots relative intensity of parent ions (created in an EI source at 3 V offset voltage) as a function of the pretrapping potential of the front ICR-cell trapping plate in the range of [7, 0] volts. In these experiments the parent ions were trapped with a symmetric trapping potential of 10 volts. The measured dependence, $I_{par}(P_{ret})$ can be differentiated to give $G(E) = d(I_{par})/d(P_{ret})$ shown in Fig. 7(b) which is an approximate measure of the kinetic energy distribution of the parent ions. The inflection point of the S-shaped curve in Fig. 7 (a) corresponds to the maximum in Fig. 7 (b) at 3.75 eV. Because the potential sensed by all ions in the cell is altered by shifting the trapping potential in DVT the simplistic procedure of differentiation the signal is incorrect. In the Appendix we demonstrate that the simple retarding potential method if used in this case would systematically overestimate the mode kinetic energy by 0.2–0.5 eV and broaden the distribution by about

20%. Thus, for the Fig. 7 example we may conclude that the "true" most probable kinetic energy of parent ions exceeds the source block offset potential (3 V) by about 0.5 eV. Further the (KED) has a width of about 2.6 eV FWHM, and about 5 eV full range, in good correspondence with that expected for 3 V settings of the source block and 5 V repeller.

An obvious artifact in the energy distribution is the shoulder of the KED extending below 3 eV. The width and mean value are reasonable for the experimental source parameters employed but the extension of the distribution to energies lower than the source block potential was unexpected and is not readily explained. The open structure of the source and poor collimation of the electron beam, along with weak extraction fields employed, suggest that ions are formed throughout the ion source volume. Further, electrostatic field distribution in the source is not well defined. One can speculate that the ion extraction occurs when space charge trapping by electrons is overcome by positive space charge as ions accumulate and repels ions from the source once they surmount the trapping potential. This can account for a shift of several tenths of an eV in the effective potential of the source volume but cannot account for a shift of the order of 2 eV implied by Fig. 7.

Energy loss processes in ion injection would also shift the curve to lower energy. Collisions in the vicinity of the relatively open source are a plausible loss mechanism. In addition, ions which are not centered when they traverse the ICR cell entrance aperture experience a field gradient orthogonal to the cell axis which can convert axial translational motion into cyclotron motion. Finally, any experimental error in the Fig. 7(a) retarding potential plot is exaggerated by differentiation in Fig. 7(b). The relative contributions of these sources to the energy width cannot be reliably estimated and we take the conservative approach that the ion beam energy is equal to the nominal source potential and has a FWHM equal to 2.6 eV, the value deduced from Fig. 7(b).

With only the modest variation described in the Experimental section essentially the same retarding potential technique was used to deduce approximate velocity distributions for the fragment ions. For many reasons the characterization of fragment ion kinetic energy distributions is much more complicated than characterizing the primary ion beam. The primary ion beam is well collimated and a relatively steep retarding potential on the end cap of the ICR cell reverses the velocity vector, which (with the possible exception of ions which are orthogonally accelerated and convert axial motion into cyclotron motion described above) remains well-aligned with the axis of the cell. However, ions which collide with and recoil from the surface will have a range of recoil velocities and a distribution of velocity components parallel and perpendicular to the magnetic field axis. The perpendicular component appears as cyclotron motion and the radial position of the surface hit combined with the electrostatic field curvature at that point will determine the magnetron orbit. Further, recoiling ions with sufficient internal energy to decompose generate another randomized distribution of velocity vectors. Any recoil energy as the product ion and neutral fragments separate from their common center of mass is partitioned between the two particles with conservation of momentum. The resulting kinetic energy of the ion adds vectorially to the precursor ion velocity vector. The situation is further complicated by DVT when the trapping plates potentials are pulsed to a positive value to capture ions. The potential of the entire cell and the gradient of potential within the cell are shifted. Both the potential and kinetic energy of the ions is position dependant and must be evaluated in the analysis of the experimental retarding potential curves.

The general algorithm of the DVT-KED-deduction method described in detail in the Appendix is iterative and similar to that used in RIEDS. In the first step we guess the initial kinetic energy distribution of the ion; for a trial function F(E) we assume a Boltzmann distribution. Secondly, we calculate the axial-ion-density function, D(z) which is inversely proportional to ion velocity as the ions move inside the ICR cell. Finally we estimate the dynamic increase in the mechanic energy of the ions located along the z axis when the DVT is activated. We define a "capture criterion" that total energy of the ion must be lower than the DVT potential. The total number of ions with

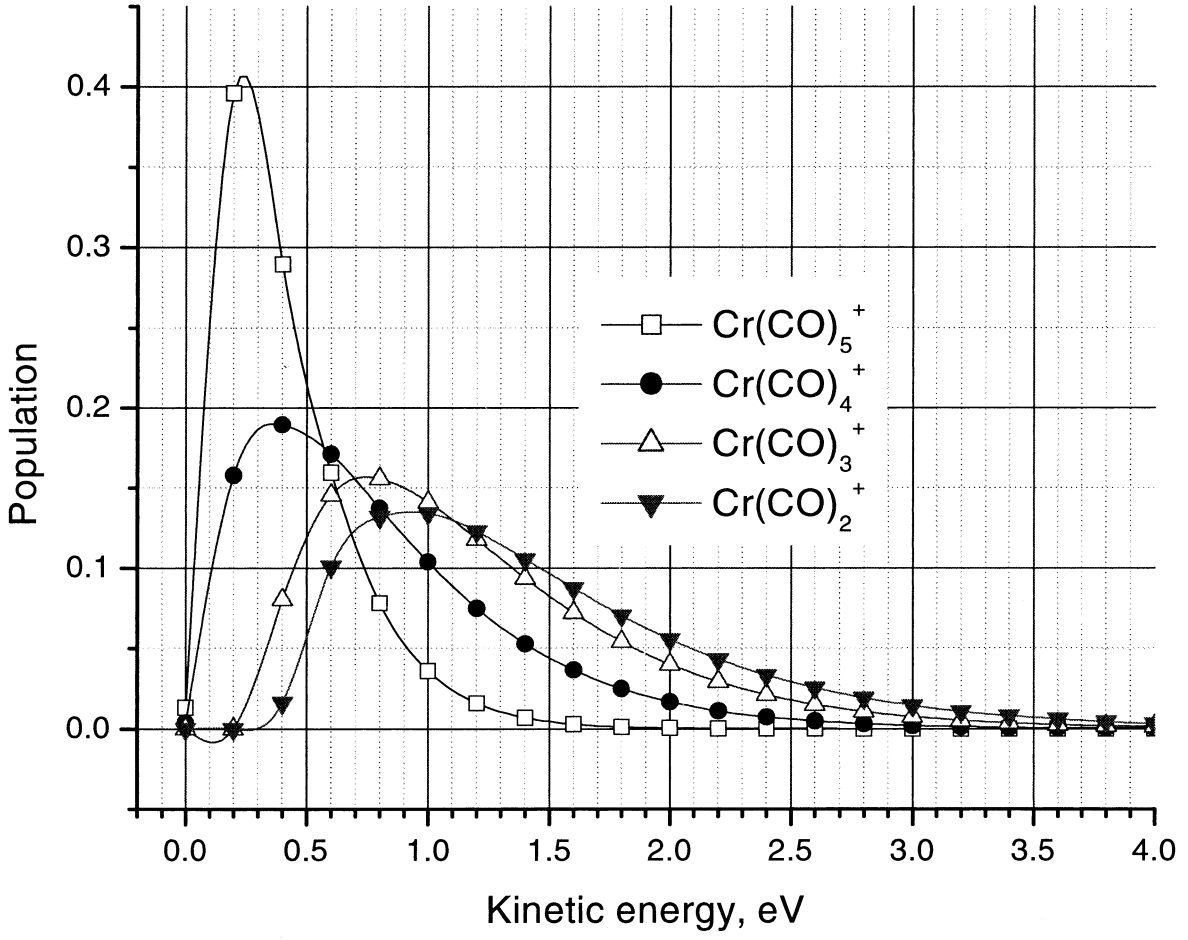

Fig. 8. Fragment ion KEDs predicted by the kinetic energy deduction method described in the Appendix for four fragments of $Cr(CO)_6^+$ at 7 eV SID. Source block offset voltage was 10 volts and front- and back-trapping plates potentials were 0 and 3 volts, respectively, prior to activation of varied-level DVT.

a trial kinetic energy distribution which can be captured is calculated as a double integral over axial coordinate, z and initial kinetic energy, E, of the product of two probability functions: F(E) and D(z) with the upper limits of integration dictated by the capture criterion. This theoretically predicted number of ions captured is calculated for each dynamic trapping voltage. The resulting theoretical "curve" of ion-abundance dependence on the trapping voltage is compared with the experimental ion abundance-on-DVT curve. The residuals are estimated and the trial kinetic energy distribution function is adjusted by SIMPLEX, updating the trial-function parameters. The calculations are repeated until the set of parameters of the trial function gives the best fit between the calculated and experimental curves of ion abundance versus DVT.

Results of converged Boltzmann-type F(E) distributions for four fragments at 7 eV SID are shown in Fig. 8. It should also be noted that evidently the energy distributions of fragment ions did not depend noticeably on the collision energy; at 15 and at 7 eV SID, for example, the relative ion abundances of the fragments are different, but the KED for each fragment is essentially unchanged. Important conclusions drawn from this result are that kinetic energy of all

fragment ions is relatively low and weakly depend on collision energy. Secondly, the lighter fragments have higher kinetic energies: the most probable energy shifts upwards with decreasing mass.

The later conclusions are further analyzed, as follows: in unimolecular decay of a precursor ion of mass M_0 into fragments of masses m and M_1, the velocity of fragment M_1, with respect to the velocity of the decomposing ion, M_0, is

$$V_{M_1} = \frac{\sqrt{2E_0\mu_1}}{M_1}, \quad (4)$$

where $\mu_1 = mM_1/M_0$ is the reduced mass, V_{M1} is the center of mass velocity of M_1, and E_0 is the kinetic energy released by the dissociation. In the LAB frame, the front- and back-scattered fragment velocities add to the original velocity V_{M0} of the parent ion recoiling from the surface. The maximum (+) and minimum (−) axial velocity components of kinetic energy are

$$T_{\pm,z}(M_1) = \frac{M_1\,(V_{M_0,z} \pm V_{M_1})^2}{2}$$

$$= \frac{M_1\,V_{M_0,z}^2}{2} + \frac{E_0\mu_1}{M_1} \pm V_{M_0,z}\,\sqrt{2E_0\mu_1} \quad (5)$$

The overall axial kinetic energy is distributed uniformly between $T_{-,z}$ and $T_{+,z}$ [32]. This result applies to collision-free ion traps. In sector instruments the radially scattered ions can be lost for detection and the front- ($T_{+,z}$) and back-scattered ($T_{-,z}$) peak positions and shapes are analyzed to study the decomposition energetics. In ICR experiments all the ions, even the ions with significant radial velocity-component are confined to finite cyclotron orbits. Ions which are scattered close-to-orthogonal with respect to the parent ion velocity may gain significant cyclotron motion but will experience little change in their CM z-axis energy component and remain available for ICR detection. Thus the uniform distribution between $T_{-,z}$ and $T_{+,z}$ should directly translate into the uniform distribution of the detected fragments between the least energetic and the most energetic ones. This difference between sectors and ion trap instruments in terms of KED of unimolecular decay products is a fundamental property of the two types of mass analyzers. The sector instrument may detect the two-peak front- and back-scattered decomposition pattern along the kinetic energy axis, while the ICR experiment, in principle, always provides a perfect square for the kinetic energy distribution of the fragment ions.

Implications of Eq. (5) for the KED of the fragment ions detected in SID ICR experiment are best understood by considering the terms individually. The third term of the sum on the right in Eq. (5) is responsible for peak broadening, while the first and second terms determine the centroid of the energy distribution, $<T_z>$. The first term, proportional to the fragment ion's mass, M_1, arises from the precursor ion LAB-frame surface-recoil velocity, V. The second term, inversely proportional to M_1, results from the energy E_0 released in dissociation, specifically, recoil energy of fragment ion in the dissociation step. The width of the KED will be determined by the third term with one major correction. Namely, if kinetic energy release causes more spread in apparent kinetic energy shift than the parent ion kinetic energy (z component), the distribution is "folded" over the zero-kinetic-energy point. Finally, two additional factors smoothen the square-shaped KEDs. First, the parent ion KED contributes to the measured width. Secondly, some finite distribution of kinetic energy release (KER) should always be expected above the decomposition threshold, reflecting the probability of redistributing excess internal energy above the dissociation barrier into translation. Thus the Boltzmannlike function used in this work to model KEDs of the fragment ions is physically reasonable to approximate the final convolution product. No special emphasis on the validity of the analytical function used is made or implied.

It is interesting to compare and contrast our results shown in Fig. 8 with crossed beam studies of fragment ions in 45-degrees-collision SID [31,33,34]. In a 45-degree SID, the surface-recoiled projectile ion will have a large component velocity parallel to the surface. At high SID energies this component will be larger than any velocity gain obtained from the energy

released in dissociation. Thus the near-linear dependence of the fragment kinetic energy on mass previously reported for 45-degree-incidence SID experiments is readily explained by dissociation of a fast-recoiled precursor ion (large $M_1V^2_{M0}/2$ term, due to partial conservation of a tangential velocity component). In this case even if the kinetic-energy-release contribution, $E_0\mu_1/M_1$, is significant, its effect is lost in comparison with the first term in Eq. (5). Obviously, the near-linear dependence of fragment kinetic energy on the SID collision energy typically observed in 45-degree SID can be explained by conservation of the tangent velocity component as well [35].

3.3. Energy transfer to the surface in SID

Conservation of energy in SID collisions of an ion with initial translational energy E_{SID} requires that $E_{SID} = T_{parent} + E_{parent\ internal} + E_{surface}$, where the T_{parent} is the postrecoil translational energy of the parent ion, $E_{parent\ internal}$ is the internal (vibrational) energy of the parent ion prior to dissociation, and $E_{surface}$ is the energy lost to the surface. We assume that $E_{surface}$ represents energy dissipated in vibrational modes of the SAM polymer. This may further result in SAM fragmentation, substrate heating, ejection of excited neutrals, etc.; which are not detected in our experiments and not discussed further.

Once the internal energy of the recoiled parent is estimated, we can deduce from energy balance the energy lost to the surface, $E_{surface}$ as a function of collision energy. Based on the assumption that T_{parent} is negligible energy transfer into the surface as a function of collision energy is presented in Fig. 9. The dashed line corresponds to transfer of all the kinetic energy of the projectile ion into $E_{surface}$. This line may also be considered the "capture limit" in which the ion is trapped by molecular interactions with the SAM polymer structure. Neglecting the recoil kinetic energy of the precursor ion entirely is incorrect for low energy SID, and rigorous measurements of kinetic energy in the low collision energy region might well displace the experimental $E_{surface}$ slightly below the "ideal heating" curve at low energies. For this reason we cannot be sure that the experimental, solid line is not essentially parallel to the dashed line at very low SID energies. Despite this limitation it is clear from Fig. 9 that most of the projectile ion kinetic energy is dissipated in the surface and is definitely not retained as internal energy in the recoiling ion. We also note that of the order of 70% of impacting ions are "lost" in processes discussed in Sec. 1 and are not included in this analysis of energy disposition.

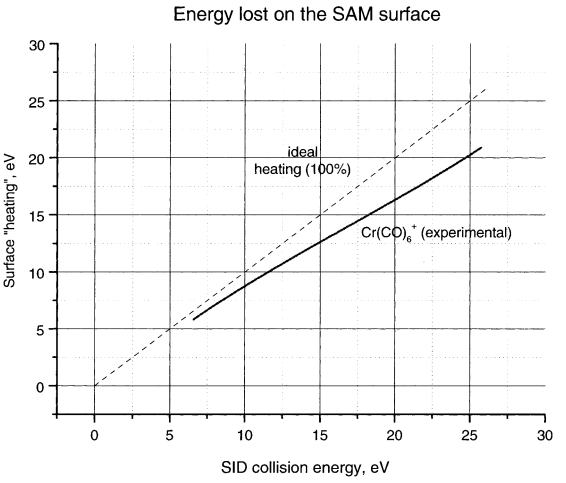

Fig. 9. Energy transfer to the surface deduced from energy balance using the T-V transfer efficiency when postsurface recoil kinetic energy of the parent ion is disregarded. The dashed line represents expected result if all the primary ion kinetic energy is transferred to the surface; the actual curve is lower. The difference between the two determines energy deposited into translation and vibration of the recoiled parent ion.

4. Conclusions

The focus of this research is energy transfer process in activation of ions through their collision with a fluorinated SAM surface. Determining energy deposition in the collision process is a necessary step in achieving a fundamental understanding of SID activation processes. Although SAM surfaces strongly suppress ion neutralization (when compared to bare metal surfaces, oil-film-coated surfaces or organic layers) neutralization remains the dominant reaction of organic ions striking a surface with moderate kinetic energy. For ions which are neither neutralized nor surface captured, internal excitation is much more

probable than reaction for the fluorinated surface considered here. Remarkably little of the ion kinetic energy is preserved as kinetic energy of the recoiling ion. For all ions the collision process represents a "sticky collision" with efficient deposition of kinetic energy into surface modes. Indeed, most of the ions are "stuck" or neutralized and do not leave the surface as ions. For those which do, SID with a fluorinated SAM surface is remarkably efficient in maximizing energy flow into internal modes and minimizing translational energy of the recoiling ion.

The sum intensities of fragment ions was of the order of 30% of the parent ion intensity when freshly prepared surfaces were used. The kinetic energy of SID fragments was determined by deducing kinetic energy distributions from experimental ion abundance at various trapping potentials and was found to increase with decreasing fragment mass. The parent ion kinetic energy following recoil from the target and prior to dissociation was shown to be much smaller than internal energy deposited in the recoiling ion. This is consistent with a collision mechanism involving rapid fragmentation of slowly recoiling parent ions. The efficiency of translational-to-vibrational energy transfer in the SID event was measured in the range of SID collision energy from 0 to 25 eV and found to be collision energy dependent. It maximizes at about 19% at 23 eV SID collision energy. Energy lost to the SID target surface was shown to be the dominant energy sink in ion-surface collisions.

Acknowledgments

Collaboration in instrumental modifications with the R&D and Customer Support groups of Bruker Daltonics and scientific cooperation with Professor Vicky Wysocki and her research group at the University of Arizona are greatly acknowledged. Detailed discussions with Visiting Professor Eugene Nikolaev and Drs. Steven Barlow and Julia Laskin at PNNL were extremely useful in interpreting our data. We gratefully acknowledge financial support from DOE Grant DE-FG02-97ER14813 to the University of Delaware and resources provided by Environmental Molecular Science Laboratory User Facility at PNNL. We are also grateful to a referee of this paper who pointed out problems in a simplistic interpretation of our experiments by retarding potential method.

Appendix

The kinematics of the ions trapped in the ICR cell using dynamic voltage trapping (DVT) as described in the Instrumental section was modeled using the formalism presented here. A number of simplifications to the true physical model are made to make it tractable without sacrificing the accuracy of the result. We begin by asserting that the time duration of impacting parent ions onto the SID target is much longer then the time the ions spend traveling through the cell so that the ion beam may be considered continuous. This approximation clearly applies to our experiments where the parent ion beam was directed onto the surface for about 1 ms and the flight time in the cell was on the order of 50 μs (based on SIMION simulations) under typical conditions of 15 volts source block potential offset and 0 and 3 volts applied to the front and the back trapping plates, respectively. Thus at the time of DVT activation, a steady-state spacial distribution of the ions (both parent and fragments) which is dictated only by cell potentials and ion kinetic energy content is assumed. Secondly, the ion motion is assumed axial. This approximation significantly simplifies the analysis of the kinetic energy distribution of fragment ions, but its validity and sensitivity of the model to nonaxial velocity components in a 7 T magnetic field have not been examined. We further assume that the potential inside the ICR cell is changed instantly when DVT is activated. Quantitatively this requires that the time for the potential change be shorter than the time it takes the ions to move to a significantly different potential. This criterion is relatively easily met with fast voltage-switch electronics in our ICR cell geometry and for ions of our *m/z* range. Under this assumption the energy gained by the ions is given by the change of potential at the point where they are located when DVT is activated.

The abundance of fragment ions clearly depends on the voltages used to trap them for ICR excitation and detection after the surface hit. In our fragment ion KED studies, the ion source and optics conditions are kept unchanged from experiment to experiment, but the DVT level is varied. Typically the fragment ion abundance in the detected spectrum increases rapidly with trapping voltage up to a certain inflection point, after which the increase slows and plateaus. The ion abundance flattens when the DVT voltage is higher than the maximum translational energy of the ions and all of them are successfully captured. The characteristic inflection point roughly indicates (but overestimates) the most probable translational energy of the ion. However, when the axial potential distribution in the ICR cell changes rapidly, as in the case of the DVT activation, the ions distributed along the axis inside the cell will acquire energy from the potential change corresponding to their axial position. For "ideal" excitation/detection, when every captured ion is detected, the dependence of ion abundance on the DVT potential is defined by the on-axis potentials before and after the DVT activation, the ion population along the axis and the kinetic energy of the ions prior to DVT activation.

The general expression for the potential on axis created by trapping plates potentials [36,37] is

$$V(x) = \frac{2}{\sqrt{(\pi)}} \sum_{s=1}^{\infty} \frac{V_1\, sh\left(\frac{x + x_t}{\rho} j_s\right) - V_2\, sh\left(\frac{x - x_t}{\rho} j_s\right)}{J_1\,(j_s)\, sh\left(2\frac{x_t}{\rho} j_s\right)} \tag{A1}$$

where $x = 0$ in the center of the cell, ρ is the cell diameter, V_1 and V_2 are the potentials on the trapping plates at x_t and $-x_t$, J_1 is the cylindrical Bessel function of first kind of first order, and j_s is the solution to J_0 of zero order. Eq. (A1) is ideal for estimating the potentials near the center of the cell numerically. Unfortunately with any finite number of members in the sum over s this function goes to minus infinity as x closely approaches x_t from below or $-x_t$ from above. This makes any computer simulation physically invalid in the vicinity of the trapping plates, exactly where most of our fragment ions are situated.

For this reason the on-axis potentials of our ICR cell with its aspect ratio of 1 were modeled using the SIMION program and approximated with physically nonmeaningful, but numerically simple polynomials, as shown in Fig. 8. The two curves correspond to on-axis potentials realized when the front and the back trapping plates are kept at 0 and 3 volts [squares, $P^0\,(z)$] and 3 and 3 volts [circles, $P^1\,(z)$], respectively. The z coordinate of the back trapping plate where the ions are born is 0, and the front trapping plate is situated at $z = 60$ (mm). Potentials applied to the front and the back trapping plates in both cases can be expressed then as $P^0\,(60)$, $P^0\,(0)$, $P^1\,(60)$, and $P^1\,(0)$. We will call DVT symmetric if $P^{dvt}\,(z) = P^{dvt}\,(60 - z)$, which is realized if front and back trapping plates have the same potential [like the one represented by $P^1\,(z)$, where $P^1\,(0) = P^1\,(60) = 3$ V]. By electrostatic field superposition the symmetric DVT by any potential other then 3 volts will scale the potentials linearly from $P^1\,(z)$, according to:

$$P^{dvt}\,(z) = P^1\,(z)\,\frac{P^{dvt}\,(0)}{P^1\,(0)} = P^1\,(z)\,\frac{P^{dvt}\,(0)}{3V} \tag{A2}$$

Fig. 10 illustrates an algorithm for deducing fragment ion kinetic energy distributions from the dependence of ion abundance on the trapping voltage. Fragment ions are assumed to be originate on the surface at the potential of $P_0(0) = 3$ V. This is valid in case of rapidly decomposing parent ions, such as $Cr(CO)_6^+$ investigated in our research. Initially they have a distribution of kinetic energies $F^0\,[E^0_k(0)]$. Let us assume it is Boltzmannlike;

$$F^0\,[E^0{}_k(0)] = F^0\,(x) = \begin{cases} k_1\,(x_1 - x_0)\, e^{-k_2\,(x - x_0)}, & x > x_0 \\ 0, & x < x_0 \end{cases} \tag{A3}$$

where k_1, k_2, and x_0 are parameters. The total energy of a fragment ion upon its birth is

$$E^0{}_{tot}(0) = P^0(0) + E^0{}_k(0) \tag{A4}$$

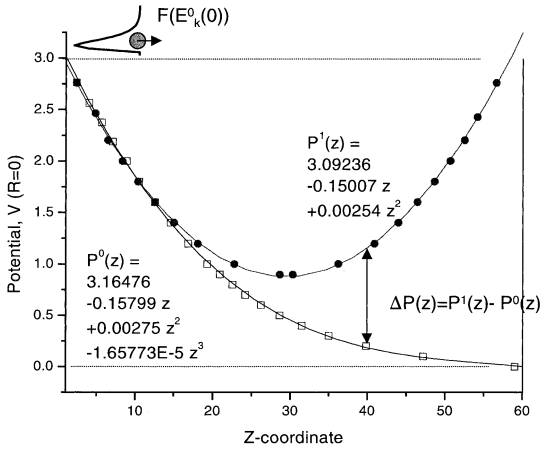

Fig. 10. Fragment ion KED-deduction method illustration: the curve marked with squares is the on-axis potential when the trapping plates are kept at 3 and 0 volts for back- and front-trapping plates, respectively. The curve with circles corresponds to symmetric DVT of 3 volts. The F(Ke) depicts the assumed post-SID kinetic energy distribution, when Ke energy is added to the T component acquired from potential gradient along the trajectory, ΔP is the energy deposited into the system when the potential is instantly switched from bottom to top curve.

As the ions travel away from the back-trapping plate additional kinetic energy is acquired as the ions travel through region of lower potential. The kinetic energy becomes $E^0{}_k(z) = E^0{}_k(0) + P^0(0) - P^0(z)$ while the total energy is unchanged:

$$E^0{}_{tot}(z) = E^0{}_{tot}(0) = P^0(z) + E^0{}_k(0) + P^0(0) - P^0(z) = P^0(z) + E^0{}_k(z) \quad \text{(A5)}$$

The ions axial density distribution is proportional to the time the ions spent at a given coordinate. This time is inversely proportional to ions velocity, which can be obtained from its kinetic energy at z:

$$D[z, E^0{}_k(0)] \sim t[z, E^0{}_k(0)] - \frac{1}{v[z, E^0{}_k(0)]} = \sqrt{\frac{m}{2\,E^0{}_k(z)}} = \sqrt{\frac{m}{2[E^0{}_k(0) + P^0(0) - P^0(z)]}} \quad \text{(A6)}$$

When DVT is activated the $P^{dvt}(0)$ potential is applied *instantly* to both trapping plates. Under this condition kinetic energy of the ion is *unchanged* but the total energy of the ion is increased by $\Delta P(z) = P^{dvt}(z) - P^0(z)$, the difference between the potentials at the ion location before and after DVT (see Fig. 10 for DVT of 3 V). The new total energy of the ion is

$$E^1{}_{tot}(z) = E^0{}_{tot}(z) + \Delta P(z) = E^0{}_{tot}(0) + P^{dvt}(z) - P^0(z) \quad \text{(A7)}$$

Combining Eq. (A7) with (A4) and (A2) we can formulate the criterion for an ion to be captured: it's total energy after DVT activation $E^1{}_{tot}(z)$ must not exceed the trapping potentials $P^{dvt}(0) = P^{dvt}(60)$:

$$P^0(0) + E^0{}_k(0) + P^1(z)\frac{P^{dvt}(0)}{P^1(0)} - P^0(z) \le P^{dvt}(0) \quad \text{(A8)}$$

In terms of initial kinetic energy of the ion it reads:

$$E^0{}_k(0) \le P^{dvt}(0)\left[1 - \frac{P^1(z)}{P^1(0)}\right] - P^0(0) + P^0(z) = E^{crit}{}_k(z) \quad \text{(A9)}$$

We have introduced the new value $E^{crit}{}_k(z)$ with the following physical meaning: based on the z coordinate of the ion it will be captured if it's initial kinetic energy $E^0{}_k(0)$ is lower than $E^{crit}{}_k(z)$. Thus, if the ions recoiling from the surface have initial kinetic energy distribution $F^0[E^0{}_k(0)]$ given by Eq. (A3) the captured ion ensemble will have it truncated to zero population at energies higher than $E^{crit}{}_k(z)$:

$$F^1[z, E^0{}_k(0)] = F^1(z, x) = \begin{cases} 0, & x \ge E^{crit}{}_k(z) \\ k_1 (x - x_0)\, e^{-k_2 (x - x_0)}, & E^{crit}{}_k(z > x > x_0 \\ 0, & x \le x_0 \end{cases} \quad \text{(A10)}$$

The total number of ions captured across all the z coordinates at a given DVT level is given by an integral of a product of two probability functions: the axial ion density and the kinetic energy distribution:

$$I^{capt}[P^{dvt}(0)] = \int_{z=0}^{z=60} \int_{E^0_k(z)=0}^{E^0_k(z)=E^{crit}_k(z)} F^1[z, E^0_k(0)] \, D[z, E^0] \, d[E^0_k(0)] \, dz \qquad \text{(A11)}$$

with the upper limit of integration over energy obtained from Eq. (A9) dictated by the capture criterion as outlined by the Eqs. Both distribution functions are normalized prior to truncation outlined by Eq. (A10) and calculation of the integral product.

Values of I^{capt} are calculated for all available trapping potentials,
$P^{dvt}(0)$
and the dependence of ion abundance on the trapping potential obtained theoretically as outlined above is numerically compared with the theoretical ion-abundance curve. The values for k_1, k_2, and x_0 parameters in the initial kinetic energy distribution function given by Eq. (A3) are than updated, the calculations repeated, and the comparison attempted until the residuals are minimized. The fitting procedure is similar to that used in RIEDS and the MATLAB program realizing this algorithm generates real-time screen outputs shown in Fig. 11 while the fit progresses. In Fig. 11 we used experimental data for illustration purpose. The bottom-plot curve is the currently evaluated F^0 $[E^0_k(0)]$ distribution, and the top plot depicts the corresponding ion abundances (line) calculated to fit experimental curve (circles) of $Cr(CO)_4^+$ fragment intensity in a 7 eV SID experiment (conversion interrupted) with DVT levels ranging as indicated by the top-plot abscissa. When the convergence criteria are met the resulting KED function represents the distribution which provides the best fit between the experimental and theoretically predicted dependence of the ion abundance on the trapping potential. Initial values for the parameters and the conversion level are assigned before the fit is initiated.

Fig. 12 illustrates the effect of the axial density of ions on the ions trapping efficiency. The curves plotted against the z coordinate reflect the integrals over kinetic energy of the product of truncated kinetic energy distributions [Eq. (A10)] multiplied by the ion

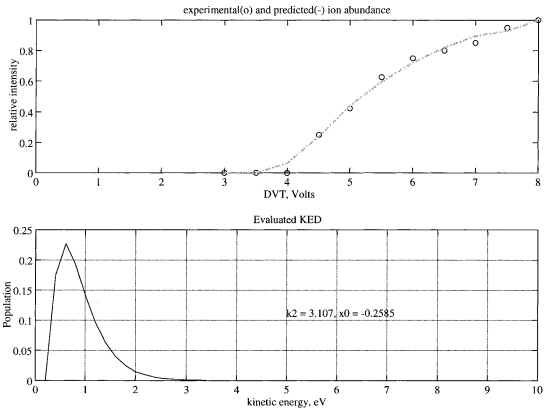

Fig. 11. Intermediate control screen output of KED-search program, realizing the deduction of F(Ke). The bottom graph plots the Ke function which is used currently to construct the dotted-line curve (on the top plot) of predicted dependence of ion abundance on DVT. The sum of squared residuals between the prediction and experimental curve (the circles) in the top plot is minimized against the parameters of the F(Ke) function using SIMPLEX search. The overall program algorithm is similar to that of RIEDS.

axial density [Eq. (A6)] for a range of trapping potentials. In estimating the total number of ions captured at a given DVT level, I^{capt} $[P^{dvt}(0)]$ as in Eq. (A11), these curves would be additionally integrated over the z coordinate. While at relatively low trapping potentials the effect of the $E^{crit}_k(z)$-based capture is prevalent, with the further increase of the trapping potential not only the region in which the ions are captured is broadened but also the relative number of ions captured near the SID origin increases. This is a direct result of lower velocity (and thus the higher density) of the ions near the SID origin.

It can be shown for our cell geometry that if pre-DVT voltage on the trapping plates is of the order of 3 volts and the DVT is at a 10 volts level approximately 90% of the ions are actually trapped. In experiments with parent ion KEDs the ions produced in the source floating at 3 volts above ground were injected into the ICR cell, whose back trapping plate was kept at 10 volts and the front trapping plate potential was systematically varied, prior to activation of 10 volts DVT on both trapping plates. Consider the situation when the front-trapping-plate barrier is at 2 volts, and the back plate is at 10 volts. The axial

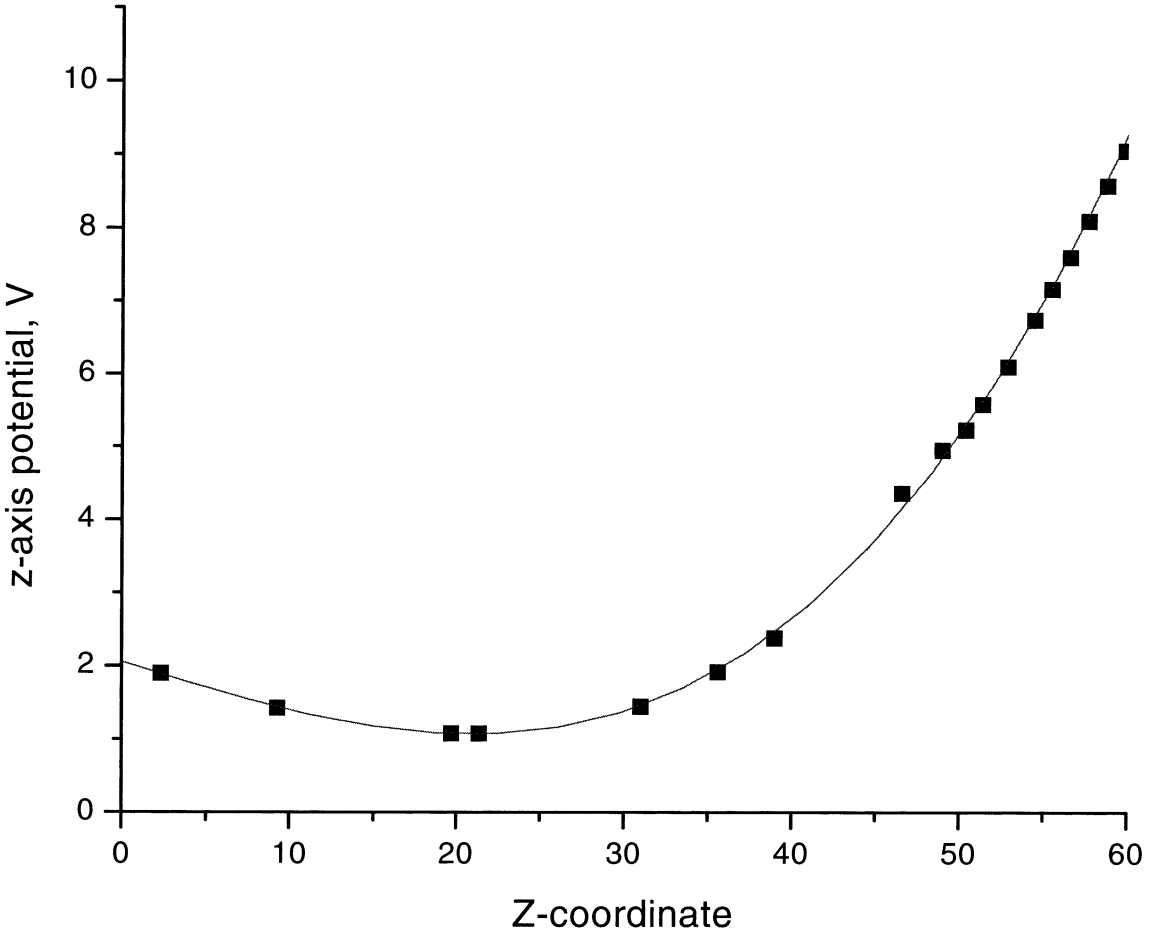

Fig. 12. On-axis potential realized when the front trapping plate is kept at 2 volts, and the back plate at 10 volts: Most of the ions which overcame the 2 volt barrier are situated near their turning point in the central region of the cell. Referring to Fig. 11(b), this is the region of most probable capture by DVT of 10 volts.

potential resulting from this setup is shown in Fig. 12. Clearly, most of the ions which are able to overcome the 2 V potential barrier will be situated far from the back trapping plate. Those ions which are close to the front trapping plate will be probably be lost when DVT is activated because of the substantial "kick" which they receive, but the majority, which situates near the turning point in the central region will be trapped. This supports our use of the traditional retarding potential method of estimating parent ion kinetic energy by the inflection point of ion abundance.

Errors resulting from using this approximate measure of KEDs can be estimated using the analysis presented in Fig. 11. Differentiating the dashed line from the top plot simulates the approximate method for deducing KEDs which we used in the analysis of parent ion kinetic energy. By comparing this result with the theoretical kinetic energy distribution function from the bottom plot we conclude that the approximate method systematically overestimated the mode and the breadth of the distribution. The breadth of the distribution was typically overestimated by about 20%, while the most probable energy was overestimated by 10–15%. This translates into 0.1–0.5 eV positive error in assignment of the parent ion

kinetic energy at 3 eV source block potential. This error estimate of $+0.1-0.5$ eV is conserved as the source potential in increased in higher-energy SID experiments. Such accuracy is certainly sufficient to define SID collision energies in the range of source offset between 5 and 50 V. For this reason no KED deduction was used in the parent ion kinetic energy analysis reported in the main text of our paper.

References

[1] R.G. Cooks, T. Ast, Md.A. Mabud, Int. J. Mass Spectrom. Ion Processes 100, (1990) 209.
[2] T. Zhang, Ph. D. Thesis, University of Delaware, 1995.
[3] R. Worgotten, J. Kubista, J. Zabka, Z. Dolejsek, T.D. Mark, Z. Herman, Int. J. Mass Spectrom. Ion Processes 174 (1998) 53.
[4] A.D. Sen, H.L. de Clercq, V.S. Rakov, A.K. Shukla, J.H. Futrell, Proceedings of the 46th ASMS Conference on Mass Spectrometry Allied Topics, 1998, p. 73.
[5] R.D. Beck, J. Rockenberger, P. Weis, M.M. Kappes, J. Chem. Phys. 104 (1996) 3638.
[6] W.R. Koppers, K. Tsumori, J.H.M. Beijersbergen, T.L. Weeding, P.G. Kistemaker, A.W. Kleyn, Int. J. Mass Spectrom. Ion Processes 174 (1998) 11.
[7] W.R. Koppers, J.H.M. Beijersbergen, T.L. Weeding, P.G. Kistemaker, A.W. Kleyn, J. Chem. Phys. 107 (1997) 10736.
[8] W.R. Koppers, M.A. Gleeson, J. Lourenco, T.L. Weeding, J. Los, A.W. Kleyn, J. Chem. Phys. 110 (1999) 2588.
[9] S.B.M. Bosio, W.L. Hase, Int. J. Mass Spectrom. Ion Processes 174 (1998) 1.
[10] D.G. Schultz, S.B. Wainhaus, L. Hanley, P. de Sainte Claire, W.L. Hase, J. Chem. Phys. 106 (1997) 10337.
[11] C.F. Ijames, C.L. Wilkins, Anal. Chem. 62 (1990) 1295.
[12] J.A. Castoro, L.M. Nywaysir, C.F. Ijames, C.L. Wilkins, Anal. Chem. 64 (1992) 2238.
[13] J.A. Castoro, P.V. Rucker, C.L. Wilkins, J. Am. Soc. Mass Spectrom. 3 (1992) 445.
[14] R.A. Chorush, D.P. Little, S.C. Beu, T.D. Wood, F.W. McLafferty, Anal. Chem. 67 (1995) 1042.
[15] B.E. Winger, R.K. Julian, Jr., R.G. Cooks, C.E.D. Chidsey, J. Am. Chem. Soc. 113 (1991) 8967.
[16] V.H. Wysocki, J.L. Jones, J.M. Ding, J. Am. Chem. Soc. 113 (1991) 8969.
[17] M. Morris, D.E. Riederer, Jr., B.E. Winger, R.G. Cooks, T. Ast, C.E.D. Chidsey, Int. J. Mass Spectrom. Ion Processes 122 (1992) 181.
[18] A. Somogyi, T.E. Kane, J.M. Ding, V.H. Wysocki, J. Am. Chem. Soc. 115 (1993) 5275.
[19] T.E. Kane, A. Somogyi, V.H. Wysocki, Org. Mass Spectrom. 28 (1993) 283.
[20] M.D. Porter, T.B. Bright, D.L. Allara, C.E.D. Chidsey, J. Am. Chem. Soc. 109 (1987) 3559.
[21] L. Strong, G.M. Whitesides, Langmuir 4 (1988) 546.
[22] H.O. Finklea, D.D. Hanshew, J. Am. Chem. Soc. 114 (1992) 3173.
[23] W. Zhong, E.N. Nikolaev, J.H. Futrell, V.H. Wysocki, Anal. Chem. 69 (1997) 2496.
[24] V.S. Rakov, J.H. Futrell, E.V. Denisov, E.N. Nikolaev Eur. Mass Spectrom. 6 (2000) 299.
[25] P.R. Das, T. Nishimura, G.G. Meisels, J. Phys. Chem. 89 (1985) 2808.
[26] V.S. Rakov, J.H. Futrell, E.N. Nikolaev, J. Wronka, Proceedings of the 46th ASMS Conference on Mass Spectrometry Allied Topics, 1998, p. 901.
[27] V.H. Wysocki, H.I. Kenttamaa, R.G. Cooks, Int. J. Mass Spectrom. Ion Processes 75 (1987) 181.
[28] K. Vekey, A.G. Brenton, J.H. Beynon, Int. J. Mass Spectrom. 70 (1986) 277.
[29] K. Vekey, A. Somogyi, V.H. Wysocki, J. Mass Spectrom. 30 (1995) 212.
[30] W.H. Press, B.P. Flannery, S.A. Teukolsky, W.T. Vetterling, Numerical Recipes, Cambridge University Press, Cambridge, 1986.
[31] J.A. Burroughs, S.B. Wainhaus, L. Hanley, J. Phys. Chem. 98 (1994) 10913.
[32] L.D. Landau, E.M. Lifshitz, *Theoretical Physics, Vol. 1, Mechanics*, Nauka, Moscow, 1965, Chap. IV, p. 16.
[33] D.G. Shultz, H. Lim, S. Gabris, L. Hanley, J. Mass Spectrom. 34 (1999) 217.
[34] S.B. Wainhaus, H. Lim, D.G. Schultz, L. Hanley, J. Chem. Phys. 106 (1997) 10329.
[35] J. Kubista, Z. Dolesek, Z. Herman, Eur. Mass Spectrom. 4 (1998) 311.
[36] J.D. Jackson, Classical Electrodynamics, Wiley, New York, 1962.
[37] S. Barlow (to be published).